JBC Papers in Press. Published on January 28, 2006 as Manuscript M513466200
The latest version is at http://www.jbc.org/cgi/doi/10.1074/jbc.M513466200

Solution Structure of a Post-transition State Analog of the Phosphotransfer Reaction Between the A and B Cytoplasmic Domains of the Mannitol Transporter $II^{Mannitol}$ of the *Escherichia coli* Phosphotransferase System*

Jeong-Yong Suh, Mengli Cai, David C. Williams, Jr. and G. Marius Clore‡

From the Laboratory of Chemical Physics, NIDDK, National Institutes of Health, Bethesda, Maryland 20892

Running Title: Solution structure of the IIA^{Mtl}-phosphoIIB^{Mtl} complex

‡Address correspondence to: G. Marius Clore, Laboratory of Chemical Physics, Bldg 5, Rm. B1-30I, NIDDK, National Institutes of Health, Bethesda, MD 20892-0520. Tel: 301-496-0782; Fax: 301-496-0825; E-mail: mariusc@intra.niddk.nih.gov.

The solution structure of the post-transition state complex between the isolated cytoplasmic A (IIA^{Mtl}) and phosphorylated B (phosphoIIB^{Mtl}) domains of the mannitol transporter of the *Escherichia coli* phosphotransferase system has been solved by NMR. The active site His-554 of IIA^{Mtl} was mutated to glutamine to block phosphoryl transfer activity, and the active site *Cys-384* of IIB^{Mtl} was substituted by serine to permit the formation of a stable phosphorylated form of IIB^{Mtl}. The two complementary interaction surfaces are predominantly hydrophobic, and two methionines on IIB^{Mtl}, *Met-388* and *Met-393*, serve as anchors by interacting with two deep pockets on the surface of IIA^{Mtl}. With the exception of a salt bridge between the conserved Arg-538 of IIA^{Mtl} and the phosphoryl group of phosphoIIB^{Mtl}, electrostatic interactions between the two proteins are limited to the outer edges of the interface, are few in number and appear to be weak. This accounts for the low affinity of the complex (K_{diss} ~3.7 mM) which is optimally tuned to the intact biological system in which the A and B domains are expressed as a single polypeptide connected by a flexible 21 residue linker. The phosphoryl transition state can readily be modeled with no change in protein-protein orientation and minimal perturbations in both the backbone immediately adjacent to His-554 and *Cys-384* and the side-chains in close proximity to the phosphoryl group. Comparison with the previously solved structure of the IIA^{Mtl}-HPr complex reveals how IIA^{Mtl} uses the same interaction surface to recognize two structurally unrelated proteins, and explains the much higher affinity of IIA^{Mtl} for HPr than IIB^{Mtl}.

The bacterial phosphoenolpyruvate:sugar phosphotransferase system (PTS)[1] comprises a fundamental signal transduction pathway whereby phosphotransfer via a series of biomolecular steps is coupled to sugar transport across the membrane (1-4). The phosphoryl group originates on phosphoenolpyruvate and the initial transfer steps, involving first enzyme I and subsequently HPr, are common to all components of the pathway. Thereafter the phosphoryl group is transferred to sugar specific enzymes II, of which there are four major classes, glucose (Glc), mannitol (Mtl), mannose (Man) and chitobiose (Chb), which share no sequence similarity to one another (2,3), and with one exception (the B domains of enzymes II^{Mtl} and II^{Chb}) no structural similarity to one another either (4-15). Enzymes II generally comprise three domains, two cytoplasmic, A and B, and one transmembrane, C, which may or may not be covalently linked to one another (2-4). The A domain accepts the phosphoryl group from HPr and donates it to the B domain. Subsequently the phosphoryl group is transferred from the B domain to the incoming sugar bound to the C domain. The complexes of the PTS are of considerable interest from the perspective of protein-protein interactions since similar binding surfaces can recognize multiple, structurally different, targets. We have embarked on a long-term structural study of the complexes of the PTS, and to date we have determined the solution NMR structures of the enzyme I(EI)-HPr complex (16), complexes of HPr with IIA^{Glc} (17), IIA^{Mtl} (18) and IIA^{Man} (19), and the complex of IIA^{Glc} with IIB^{Glc} (195. In this paper we present the solution structure of a post-transition state analog of the IIA^{Mtl}-IIB^{Mtl} complex. Specifically, we make use of the active site *C384S* mutant of IIB^{Mtl} to generate a stably phosphorylated form IIB^{Mtl} (20,21), and the active site H554Q mutant of IIA^{Mtl} to prevent phosphoryl transfer between IIA^{Mtl} and IIB^{Mtl}. (Throughout the text and figures, residues of IIB^{Mtl} are denoted in *italics*.) The complex reveals the structural basis of specific

recognition between IIA^{Mtl} and IIB^{Mtl} and the interactions involved in phosphoryl transfer.

EXPERIMENTAL PROCEDURES

Cloning, Expression, and Purification of IIA^{Mtl}(554Q) and phosphoIIB^{Mtl}(C384S) – The region corresponding to the A domain (IIA^{Mtl}) of the mannitol transporter, residues 490-637, was cloned as described previously (18). From this original construct, the active site histidine residue (His-554) was mutated to a glutamine to disable its phosphoryl transfer activity. The new construct was verified by DNA sequencing, and then subcloned into a modified pET-32a vector (14) to form a thioredoxin fusion protein with a 6-His tag. After transformation with an expression vector, *E. coli* strain BL21(DE3) (Novagen) was grown in either Luria Bertini or minimal media (with $^{15}NH_4Cl$ and/or $^{13}C_6$-glucose as the sole nitrogen or carbon sources, respectively), induced with 1 mM isopropyl-β-D-thiogalactopyranoside at an $A_{600} \sim 0.8$, and harvested by centrifugation after 4 h of induction. After harvesting, the cell pellet was resuspended in 50 ml (per liter culture) of 50 mM Tris, pH 7.4, 100 mM NaCl, 2 mM β-mercaptoethanol, 10 mM imidazole, and 1 mM phenylmethylsulfonyl fluoride. The suspension was lysed by three passages through a microfluidizer, and centrifuged at 10,000 x g for 20 minutes. The supernatant fraction was loaded onto a nickel-Sepharose column (~20 ml; Amersham Biosciences), and the fusion protein was eluted with a 100-ml gradient of imidazole (25mM to 500 mM). The fusion protein was then dialyzed against 20 mM Tris, pH 8.0, 200 mM NaCl, and 2 mM β-mercaptoethanol, and digested with thrombin (10 NIH units/mg of protein). Thrombin was removed by passage over a benzamidine-Sepharose column (1 ml; Amersham Biosciences) followed by the addition of 1 mM phenylmethylsulfonyl fluoride. The cleaved 6-His-thioredoxin was removed by loading the digested proteins over a nickel-Sepharose column. IIA^{Mtl}(H65Q) was further purified by Sephadex-75 gel filtration column (Amersham Biosciences) equilibrated with 20 mM Tris, pH 7.4, 1 mM EDTA, and 0.01 % (w/v) sodium azide.

The active site mutant of the B domain, IIB^{Mtl}(*C384S*), of the mannitol transporter (residues 375-476) was cloned, expressed, phosphorylated, and purified as described previously (21).

With the exception of the titration experiments, NMR samples contained 3 mM IIA^{Mtl}(H65Q) and 3mM phosphoIIB^{Mtl}(*C384S*) in 20 mM tris-d_{11} (pH 7.4), 0.01% (w/v) sodium azide, and either 90% H_2O/10% D_2O or 99.996% D_2O. Each sample contained complexes of one uniformly ^{15}N /^{13}C-labeled protein with its unlabeled partner. For titration experiments, 0.6 mM of either protein was titrated with the other protein using up to 1:12 molar ratios in 20 mM tris, pH 7.4, and 0.01% (w/v) sodium azide.

NMR Spectroscopy – NMR spectra were collected at 30°C on Bruker DRX800, DMX750, DMX600, DRX600 and DMX500 spectrometers equipped with either an *x,y,z*-shielded gradient triple resonance probe or a *z*-shielded gradient triple resonance cryoprobe. Spectra were processed with the NMRPipe package (22), and analyzed using the program PIPP/CAPP/STAPP (23).

Sequential and side-chain assignments of IIA^{Mtl}(H65Q) and phosphoIIB^{Mtl}(*C384S*) in a 1:1 mixture were performed using 3D triple resonance through-bond scalar correlation experiments (3D HNCACB, CBCA(CO)NH, HBHA(CBCACO)NH, C(CCO)NH, H(CCO)NH) in conjunction with 3D ^{15}N-separated, ^{13}C-separated, and $^{13}C/^{13}C$ separated nuclear Overhauser enhancement (NOE) experiments (24-26). Intermolecular NOEs were recorded with one partner $^{15}N/^{13}C$-labeled and the other unlabeled in D_2O using 3D ^{13}C-separated/^{12}C-filtered NOE experiments (26).

Side-chain torsion angle restraints were derived from $^3J_{NC\gamma}$ and $^3J_{C'C\gamma}$ coupling constants measured using quantitative J correlation spectroscopy (27) in conjunction with short mixing time (30 ms) 3D ^{13}C-separated NOE spectra recorded in H_2O (26).

Axially stretched (28) neutral polyacrylamide gels (5% w/v polyacrylamide; 39:1 w/w acrylamide/ bisacrylamide) were prepared as described previously (21). Residual dipolar couplings (RDC) were obtained by taking the difference in *J* couplings measured in aligned and isotropic (water) media. $^1J_{NH}$ couplings were determined from a 2D in-phase/anti-phase ^1H-^{15}N HSQC spectrum. Measurements on the free proteins were carried out using a protein concentration of 0.5 mM; measurements on the complex were carried out on samples containing 0.5 mM of the ^{15}N-labeled partner and 2 mM of the unlabeled partner.

Structure Calculations — NOE-derived inter-proton distance restraints were classified into loose approximate distance ranges of 1.8–2.7, 1.8–3.5, 1.8–5.0, and 1.8–6.0 Å corresponding to strong, medium, weak, and very weak NOE cross-peak intensities, respectively; an empirical correction of 0.5 Å was added to the upper distance bounds of distance restraints involving methyl groups to account for the higher apparent intensity of methyl resonances (29). NOEs involving non-stereospecifically assigned methyl, methylene, and aromatic protons were represented by a $(\Sigma r^{-6})^{-1/6}$ sum (26). The error range employed for the χ torsion angle restraints (represented by square well potentials) was $\pm 20^o$ when a unique

rotamer could be identified and ±80° when the torsion angle could be narrowed down to two of the three rotamers (19).

Structures were calculated using conjoined rigid body/torsion angle-simulated annealing (30) with the program Xplor-NIH (31). The minimized target function comprises the experimental NMR restraints (NOE-derived interproton distances, and torsion angles), a quartic van der Waals repulsion term for the non-bonded contacts (32), a multidimensional torsion angle database potential of mean force (33), and a radius of gyration potential to ensure optimal packing (34).

Structure figures were generated using the programs VMD-XPLOR (35), RIBBONS (36), and GRASP (37). Reweighted atomic probability density maps were calculated as described previously (38).

RESULTS AND DISCUSSION

Equilibrium binding of IIA^{Mtl}(H554Q) and phosphoIIB^{Mtl}(C384S) — The mannitol transporter consists of a single polypeptide comprising three independent domains (C, B and A from N to C-terminus), connected by long flexible linkers (39,40). The linker between the B and A domains is 21 residues and extends from residues 472 to 492 of the full-length protein (10,14). We studied the interaction of constructs comprising the isolated B (residues 371-474) and A domains (490-637) by ^{1}H-^{15}N correlation spectroscopy. The combined results from two titration experiments, in which phosphoIIB^{Mtl}(*C384S*) was titrated into IIA^{Mtl}(H554Q) and vice versa, are displayed in Fig. 1 Exchange between the free proteins and the complex is fast on the chemical shift scale and binding is readily monitored by following the chemical shift perturbation of the ^{15}N-labeled partner upon addition of the unlabeled second protein. The binding of the two proteins is weak and non-linear least squares optimization of all the titration data simultaneously yields an equilibrium dissociation constant, K_{diss}, of 3.7±0.2 mM. Essentially identical results were obtained using the wild type proteins.

Such weak, yet specific binding may at first appear surprising, but is in fact optimally tuned to the intact biological system. The average end-to-end distance of an unstructured 20 residue linker (given by $\sqrt{C_n n l^2}$ where n is the number of residues, C_n the characteristic ratio which has a value of ~7 for n=21, and l is the average Cα-Cα distance which has a value of 3.8 Å; ref. 41) would be expected to be ~46 Å. If one considers one of the domains to be fixed in space, then the effect of the linker is to constrain the second domain to a sphere of average volume 4.1×10^{-22} L which corresponds to an effective concentration of ~4 mM. Thus, in the intact protein one would expect the A domain to be bound to the B domain approximately 50% of the time which is perfectly reasonable given that the B domain must use approximately the same interaction surface, centered around the active site cysteine at position *384*, to accept the phosphoryl group from the A domain and subsequently transfer the phsophoryl group onto the incoming sugar on the C domain.

It is also worth noting that the intact mannitol transporter is a dimer, with dimerization occuring solely through the transmembrane C domain (42). No homodimeric interactions between A domains or B domains are likely to occur since the isolated A and B domains do not self-associate in free solution, even at high concentrations (in the millimolar range; refs. 14,18). Clearly, phosphoryl transfer between the A and B domains can occur via either intra- or intersubunit interactions between the A and B domains. Mutagenesis and complementation experiments indicate that while phosphoryl transfer can occur via both routes, intrasubunit phosphoryl transfer is dominant (43). The above argument is consistent with the latter experimental observation since the volume in which the A domain would be constrained relative to the B domain would be larger in the context of the inter- than the intra-subunit interaction, and hence the occupancy of the intersubunit IIA^{Mtl}-IIB^{Mtl} complex would be expected to be less than that of the intrasubunit complex.

Structure determination — The solution NMR structures of IIB^{Mtl} (14) and phosphoIIB^{Mtl}(*C384S*) (21) have been determined previously, and the only structural differences between the phosphorylated and unphosphorylated forms are confined to the active site loop (resides 383-393) and involve a backbone atomic rms shift of only ~0.7 Å. Extensive use of residual dipolar couplings (RDC) was made in these structure determinations (14,21), and cross-validation using RDCs in multiple alignment media (21) indicate that the accuracy of the coordinates is high, with cross-validated dipolar coupling R-factors (44) of 14-16% (in phage pf1 and neutral polyacrylamide gel) which is equivalent to values expected for 1.5-2 Å resolution crystal structures (21, 45). The crystal structure of IIA^{Mtl} has been determined at 2.0 Å resolution (10). The unit cell in the crystal comprises a dimer of dimers (note that IIA^{Mtl} does not self-associate in solution even at the high concentrations employed by NMR; ref. 18). The structure of the four molecules of IIA^{Mtl} in the unit cell are very similar with an atomic rms difference of 0.3 Å, but four regions (residues 540-543, 555-567, 580-585 and 593-599), comprising loops, exhibit differences between the two pairs of molecules in the unit cell with

maximal backbone atomic displacements in the range 1.5-3 Å. The structure of these loops in solution, both free and bound to HPr, coincides with that found in molecule D of the crystal structure as judged from residual dipolar coupling (RDC) analysis, and these 4 regions were refined independently using RDCs in two alignment media in the solution structure determination of the IIA^{Mtl}-HPr complex (18). RDCs measured in neutral polyacrylamide gel on free IIA^{Mtl}(H554Q) are in excellent agreement with the coordinates of IIA^{Mtl} in the IIA^{Mtl}-HPr complex (18) with a dipolar coupling R-factor of 17%, a correlation coefficient of 0.98, and no deviations above average for the RDCs in the region of the mutation, indicating that the structure remains unaltered within coordinate errors (45,46). Since the chemical shift perturbations for both proteins upon formation of the IIA^{Mtl}(H554Q)-phosphoIIB^{Mtl}(*C384S*) complex are very small, the largest being less than 0.3 ppm in ^{1}H (for *Asp-454* of IIB^{Mtl}) and 1 ppm in ^{15}N (for Leu-611 of IIA^{Mtl}), we conclude that the backbone of both IIA^{Mtl}(H554Q) and phosphoIIB^{Mtl}(*C384S*) remains essentially unchanged upon complex formation. Consequently, the structure determination was carried out using conjoined rigid body/torsion angle dynamics (28) based on the coordinates of free phosphoIIB^{Mtl}(*C384S*) (ref. 21; PDB accession code 1VRV) and the coordinates of IIA^{Mtl} in the IIA^{Mtl}-HPr complex (ref. 18; PDB accession code 1J6T). The coordinates of the backbone and non-interfacial side-chains were held fixed and rigid body docking with full torsional degrees of freedom for the interfacial side-chains was driven by interproton distance restraints derived from intermolecular NOE data coupled with torsion angle restraints derived from both heteronuclear coupling constant and short mixing time NOE data. Examples of the quality of the intermolecular NOE data obtained from 3D ^{13}C-separated/^{12}C-filtered NOE experiments that provide exclusively intermolecular NOEs from protons attached to ^{13}C on the ^{13}C-labeled protein to protons attached to ^{12}C on the unlabeled protein, are shown in Fig. 2. A summary of the structural statistics is given in Table I, a superposition of the backbone of the final 270 simulated annealing structures is shown in Fig. 3A and an atomic density probability map representation of some interfacial side-chains is depicted in Fig. 3B.

The NMR experiments were carried out on samples comprising a 1:1 mixture of the proteins, each at a concentration of 3 mM. Under these conditions, only 30% of each protein is in the complex. That is, the concentration of the complex in the sample is ~ 1 mM. This does not affect the observation of intermolecular NOEs. However, it does impede the use of RDCs to provide accurate and reliable information on the relative orientation of the two proteins in the complex. Since the observed RDCs in a fast exchanging system are a weighted average of the RDCs for the free and complexed protein, one could in principal back-calculate the RDCs for the pure complex on the basis of experimental RDCs measured on the free proteins and the mixture of the two proteins (19, 47). However, this requires very accurate RDC measurements under near-identical alignment conditions, as well as accurate knowledge of the fraction of bound protein. Moreover, in a mixture of labeled and unlabeled partners, the fraction of the labeled partner (on which the RDCs are measured in the mixture) should typically exceed ~30% to ensure that the complex makes a significant contribution to the observed RDCs. Because, in this instance, the two proteins bind so weakly to one another, relatively high concentrations of the unlabeled partner (>2 mM) are required. Despite attempts using a variety of alignment media, we were not able to find experimental conditions that permitted reliable back-calculation of the RDCs owing to either differential interaction of one of the partners with the alignment medium or differential perturbation of the alignment tensor by the unlabeled partner arising from molecular crowding at these protein concentrations.

Overall structure of the complex —— Ribbon diagrams providing an overall view of the complex are shown in Fig. 4. The Cα-Cα separation between the last ordered residue at the C-terminus of phosphoIIB^{Mtl} (residue *471*) and the first ordered residue of IIA^{Mtl} (residue 493) is 38 Å, a distance that can readily be accommodated by the flexible 21-residue linker. The interaction surface on IIA^{Mtl} comprises 27 residues involving three segments of polypeptide chain: residues 538 to 557 include the C-terminal end of helix α2, a small antiparallel β-sheet formed by strands β2 and β3 connected by a hairpin turn, and the active site residue at position 554; residues 480 to 585 comprise a loop connecting strands β4 and β5; and residues 598 to 612 encompass helix α3 (residues 600-610). The interaction surface on IIB^{Mtl} is made up of 18 residues located in four segments of polypeptide chain: residues *384-400* include the active site loop (residues *384-389*) and most of helix α1 (residues *390-404*); residue *414* is the C-terminal residue of strand β2; residues *430-433* make up the first turn of helix α2; and residues *451-453* are located in the loop connecting strand β4 and helix α3. The residues comprising the interaction surface of IIB^{Mtl} are highly conserved throughout gram positive and gram negative bacteria (48): 14 out of 18 residues are conserved absolutely; two are subject to highly conservative changes and preserve the functional group (*Arg-399* to lysine, *His-430* to glutamine); and one residue, *Gly-396*, can be substituted conservatively by a

serine. Only *Lys-400* is subject to non-conservative substitutions from lysine in gram negative bacteria to asparagine or aspartate in gram positive bacteria. It is also worth noting that residues *382-394* comprising the complete active site loop and the first turn of helix α1 are conserved throughout.

The interaction surfaces of IIA^{Mtl} and IIB^{Mtl} are approximately circular in shape and comparable in size (28 x 27 Å for IIA^{Mtl} and 22 x 27 Å for IIB^{Mtl}), and are composed of predominantly hydrophobic residues with 60-65% of the atoms being non-polar. The interaction surface on IIA^{Mtl} is concave while that on IIB^{Mtl} is largely convex, thereby providing overall complementarity of fit. The total accessible surface buried at the interface is 1575 $Å^2$, of which 735 $Å^2$ originates from IIA^{Mtl} and 840 $Å^2$ from IIB^{Mtl}. The gap volume index (defined as the ratio of gap volume to interface accessible surface area) is 2.7, a value typical of optional complexes, that is to say heterocomplexes where the individual components of the complex can also exit as monomers (49). The predominant intermolecular contacts between secondary structure elements involve a helix-helix interaction between helix α3 of IIA^{Mtl} and helix α1 of IIB^{Mtl}, oriented at an angle of ~60°.

The IIA^{Mtl}-IIB^{Mtl} interface — A stereoview of the interface is shown in Fig. 5 A, together with selected close-ups in Figs. 5B and 5C, surface representations of the interfaces are given in Fig. 6A, and a schematic summary of the intermolecular contacts is provided in Fig. 7. A virtually complete, horseshoe shaped ring of hydrophobic residues surrounds the active site *phosphoSer-384* of IIB^{Mtl} (Fig. 6A, bottom panel). Several intermolecular interactions are noteworthy. The two methionines on IIB^{Mtl}, *Met-393* and *Met-388*, make extensive hydrophobic contacts to residues in two deep pockets located at the top and bottom halves, respectively, of the IIA^{Mtl} interface (in the views shown in Fig. 5 and 6) that serve to anchor IIB^{Mtl} onto IIA^{Mtl}. The top pocket is formed by Leu546, Gly-547, Glu-548, Ile-550, Ile-604 and Thr-608. The bottom pocket comprises Arg-538, the active site residue Gln-554, Val-557, His-600 and Ile-601. The residues in both pockets are either conserved or substituted conservatively in gram negative and positive bacteria (48). The close contacts between *Met-338* of IIB^{Mtl} and Arg-538 and Gln-554 of IIA^{Mtl} serve to position the latter two residues such that the carboxyamide of Gln-554 is directed towards phosphoSer-384 and the guanidino group of Arg-538 makes a direct salt bridge with the phosphate group of *phosphoSer-384*. The critical role of Arg-538 is supported by its conservation throughout gram negative and gram positive bacteria, (48). The negative charge on *Asp-385*, located adjacent to *phosphoSer-384*, is partially offset by a hydrogen bonding interaction with the hydroxyl group of Thr-542. There are also a number of weak complementary electrostatic interactions, asymmetrically situated along the outer edges of the interaction surfaces that facilitate the correct orientation of the two proteins. These include interactions between *Lys-400* and Asp-612 and Asn-609, between *Arg-399* and Thr-605 and Asn-609, between *Asn-451* and Glu-582 and Asp-585, and between *His-430* and Glu-581. These electrostatic interactions, however, are likely to be relatively weak since the functional groups are separated by ≥4 Å.

The phosphoryl transition state — The phosphoryl transition state can be readily modeled by substituting Gln-554 for His and *Ser-384* for *Cys*, and minimizing the restrained regularized mean coordinates of the IIA^{Mtl}-phosphoIIB^{Mtl} complex subject to geometrical restraints for the His---phosphoryl---Cys transition state in conjunction with the experimental NMR restraints, only allowing the backbone of the active site and immediately adjacent residues (i.e. residues 383-385 of IIA^{Mtl} and *553-555* of IIB^{Mtl}) and the side-chains of the interfacial residues to move (15). The geometric restraints include N---P and S---P bond lengths, a planarity term to ensure that the phosphorus atom lies in the plane of the imidazole ring of His-554 and the sulfur atom of *Cys-384*, and bond angle terms to enforce trigonal bipyramidal geometry for the phosphoryl group (15). A dissociative transition state complex (N---P and S---P bond lengths given by the sum of the van der Waals radii of the atoms, 3.4 and 3.7 Å, respectively) can be formed with minimal atomic rms shifts of the backbone in the vicinity of the active site residues (<0.2 Å) and compensatory minor displacements of the side-chains of *Cys-384*, *Met-388*, Arg-438 and His-554 to accommodate the change in the position of the phosphoryl group (Fig. 8). An associative transition state complex (N---P and S---P bond lengths of 2.4 and 2.8 Å) can also be formed but involves slightly larger backbone displacements (0.33 Å for residues *383-385* and 0.22 Å for residues 553-555). The transition state thus preserves all the intermolecular interactions seen in the post-transition state analogue, including the neutralization of the phosphate group by the guanidino group of Arg-438. However, the hydrogen bonds to the phosphoryl group from the hydroxyl groups of *Ser-390* and *Ser-391* and from the backbone amide of *Ser-390* seen in phosphoIIB^{Mtl}(*C384S*) are no longer present in the transition state owing to the shift in the position of the phosphoryl group towards His-554 of IIA^{Mtl}.

Mechanism of phosphoryl transfer — *In vivo* phosphoryl transfer proceeds from IIA^{Mtl} to IIB^{Mtl}. A proposed mechanism for phosphoryl transfer is shown

in Fig. 9. Modeling phosphoIIA^{Mtl} on the basis of the crystal structure of IIA^{Mtl} (10) suggests that the phosphoryl group, bonded to the Nε2 atom of His-554, accepts three hydrogen bonds: two from the guanidino group of Arg-538 and a potential third from the imidazole ring of His-600 (Nε2 atom) if the χ_1/χ_2 conformation of the latter is changed from g^-/g^- (seen in the IIA^{Mtl}-phosphoIIB^{Mtl} complex) to g^+/g^-. (Note in the crystal structure of IIA^{Mtl} both rotamers are observed; ref. 10). The Nδ1-H atom of His-554 accepts a hydrogen bond from the backbone of Val-452, thereby stabilizing the Nδ1-H tautomeric state. The thiolate state of *Cys-384* of IIB^{Mtl} is stabilized by numerous hydrogen bonding interactions within the active site loop (14). Upon formation of the pre-transition state phosphoIIA^{Mtl}-IIB^{Mtl} encounter complex, the hydrogen bond between the imidazole ring of His-600 and the phosphoryl group is broken owing to steric clash with IIB^{Mtl} which precludes the g^+/g^- conformation. Nucleophilic attack at the phosphoryl group by the thiolate of *Cys-384* results in the formation of a transition state in which the phoshoryl group accepts two hydrogen bonds from the backbone amide of *Met-388* and *Gly-389* of IIA^{Mtl} and one hydrogen bond from the guanidino group of Arg-538 of IIA^{Mtl} (Fig. 8). Resolution of the transition state to the post-transition state complex results in further electrostatic interactions in which the phosphoryl group accepts five hydrogen bonds from the active site loop of IIB^{Mtl} (the backbone amides of Met-388, Gly-389, and Ser-391, and the hydroxyl groups of Ser-390 and Ser-391) and one from the guanidino group of Arg-538 of IIA^{Mtl}, and is partially neutralized by the positive helix dipole at the N-terminus of helix α1 of IIB^{Mtl}. Thus, the number of hydrogen bonding/electrostatic interactions involving the phosphoryl group in the post-transition state IIA^{Mtl}-phosphoIIB^{Mtl} complex is larger than in the pre-transition state phosphoIIA^{Mtl}-IIB^{Mtl} complex. In addition, in the transition state more hydrogen bonds to the phosphoryl group originate from IIB^{Mtl} than IIA^{Mtl}. Thus, while phosphoryl transfer between IIA^{Mtl} and IIB^{Mtl} is fully reversible *in vitro*, one would expect the flow of the phosphoryl group from IIA^{Mtl} to IIB^{Mtl} to be favored, in accord with the biological function of the PTS pathway.

Comparison of the interactions of IIB^{Mtl} and HPr with IIA^{Mtl} — A comparison of the IIA^{Mtl}(H554Q)-phosphoIIB^{Mtl}(*C384S*) and IIA^{Mtl}-HPr (18) complexes is provided in Figs. 6 and 7. Of the 27 residues of IIA^{Mtl} that interact with IIB^{Mtl}, and the 25 that interact with HPr, 23 are shared by the two interfaces (Fig. 7). Thus, IIA^{Mtl} uses essentially the same interaction surface to recognize two structurally different proteins, HPr and IIB^{Mtl}. The shape of the IIB^{Mtl} and HPr interaction surfaces are similar but bear no similarity to one another in terms of the underlying backbone topology or the orientation of secondary structure elements relative to the IIA^{Mtl} surface (Fig. 6). Indeed, helix α2 of IIA^{Mtl} lies approximately orthogonal to helices 1 and 2 of HPr (cf. top panels of Figs. 6A and B). There are, however, a number of key differences between the interaction surfaces of IIB^{Mtl} and HPr that are noteworthy. First, the number of positively charged residues on the interaction surface of IIB^{Mtl} is half that for HPr (2 compared to 4). Three of the positively charged residues on the HPr interaction surface are involved in electrostatic interactions with negatively charged residues on IIA^{Mtl}, whereas for IIB^{Mtl}, only *Lys-400* interacts with a negatively charged residue (Asp-612) on IIA^{Mtl}. This probably accounts for the much lower affinity (about 2 orders of magnitude) of the IIA^{Mtl}-IIB^{Mtl} complex relative to the IIA^{Mtl}-HPr complex (18). Second, the interaction surface on IIB^{Mtl} is significantly more hydrophobic than that on HPr (Fig. 6A and B, bottom panels). Finally, the interaction surface on IIB^{Mtl} includes a negatively charged residue (*Asp-385*), while there are no negative charges in the case of HPr. The latter is probably important in ensuring that direct interaction and phosphoryl transfer between IIB^{Mtl} and enzyme I, bypassing HPr and IIA^{Mtl}, does not occur: the presence of a negatively charged residue in close proximity to the active site residue in IIB^{Mtl} would lead to unfavorable electrostatic interactions with the interaction surface on EI that contacts HPr (16).

Comparison of the IIA^{Mtl}(H554Q)-phospho-IIB^{Mtl}(C384S) and IIA^{Glc}-IIB^{Glc} complexes — Although the A and B components of enzymes II^{Glc} and II^{Mtl} bear no sequence, secondary structure or topological similarity to one another (2,3,5,6,14,15), the two complexes share a number of features in common, as well as some significant differences. In both cases phosphoryl transfer occurs from a histidine on the A domain to a cysteine on the B domain (2,3). Unlike II^{Mtl}, the A and B domains of II^{Glc} are expressed as separate polypeptides (2,3). The general surface features of the binding interfaces on IIA^{Glc} and IIA^{Mtl} for their target proteins (HPr and the corresponding B domains) are broadly similar in terms of size and shape, each comprising a central hydrophobic region surrounding the active site residue, and an outer ring of charged residues (this paper and ref. 15). However, the IIA^{Glc} interface has a much larger preponderance of negatively charged residues (8 versus 4 for IIA^{Mt}; cf. ref. 15). The active site loops of IIB^{Glc} and IIB^{Mtl} display similarities in so far that the thiolate state of the active site cysteine is stabilized by hydrogen bonding interactions with backbone amide protons located in the

active site loop, reminiscent of the active site loop of eukaryotic protein tyrosine phosphatases (14,15). However, the structural correspondence with the latter is far more extensive for IIB^{Mtl} (14,21) than IIB^{Glc} (15). The affinity of IIA^{Glc} for IIB^{Glc} (15) is about 2 orders of magnitude higher than that of IIA^{Mtl} for IIB^{Mtl}. From a functional perspective this is fully consistent with the fact that IIA^{Glc} and IIB^{Glc} are expressed as individual proteins (2,3), whereas IIA^{Mtl} and IIB^{Mtl} are expressed as a single polypeptide chain connected by a long flexible linker (3). Examination of the two interfaces, suggests that the difference in affinities can be largely attributed to electrostatic interactions. In the case of the IIA^{Glc}-IIB^{Glc} complex there are six complementary interactions between positively and negatively charged residues (15), while there is only a single such interaction for the IIA^{Mtl}-IIB^{Mtl} complex (Fig. 6A).

Concluding remarks — The structure determination of the IIA^{Mtl}(H554Q)-phospho-IIB^{Mtl}(*C384S*) complex completes the cytoplasmic complexes of the mannitol branch of the PTS. The structure explains how IIA^{Mtl} uses the same interface to recognize both its upstream, HPr (18), and downstream, IIB^{Mtl} (this paper), interaction partners, although structurally HPr and IIB^{Mtl} are completely dissimilar, and provides a rationalization for the very different affinities of the two complexes. Thus, surface complementarity is largely achieved though hydrophobic interactions, while electrostatic interactions serve to modulate affinity. The orientation of two proteins within a protein-protein complex is clearly determined by the cumulative effect of numerous interactions, each of which makes a small contribution to the overall interaction energy. However, the structures suggest that the two complexes may use different initial determinants to drive the docking of the proteins in the correct configuration. For the IIA^{Mtl}-HPr complex it seems likely that electrostatic interactions between oppositely charged residues, distributed asymmetrically at judicious locations along the outer edge of the interaction surface may play a key role in the initial docking event. Thus a cluster of two positive charges at one edge of the HPr interaction surface (*Lys-24* and *Lys-27*) complement a cluster of two negative charges on IIA^{Mtl} (Glu591 and Asp585, respectively), while a single charge on the opposite edge of the HPr interaction surface, *Lys-49*, matches a single charge (Asp-612) on IIA^{Mtl} (Figs. 6B and 7). For the IIA^{Mtl}(H554Q)-phosphoIIB^{Mtl}(*C384S*) complex, on the other hand, the electrostatic interactions are clearly very weak, and interactions between complementary, localized hydrophobic features of the interaction surfaces may be more important, with the two conserved methionines of IIB^{Mtl} serving as hooks that latch on to the two deep hydrophobic pockets on the surface of IIA^{Mtl} (Figs. 5B, 5C and 6A). Methionine is ideally suited to such a role since its unbranched hydrophobic side-chain can sample extensive configurational space, thereby permitting optimization of its interactions with a target surface. Indeed, extensive use of methionines is employed by calmodulin to recognize many different interaction partners (50). Thus, like other complexes of the PTS, the IIA^{Mtl}(H554Q)-phosphoIIB^{Mtl}(*C384S*) complex illustrates the versatility of a protein interaction network in which each protein recognizes its upstream and downstream partner using the same interaction surface. Key features of these interactions are complementarity of shape and residue type that can be achieved using a wide array of underlying structural elements; surface side-chain conformational plasticity, particularly involving long side-chains (both hydrophobic and charged), to optimize intermolecular interactions; asymmetric distribution of complementary, intermolecular electrostatic interactions to aid in guiding correct docking; and finally extensive redundancy, thereby ensuring that the overall interaction energy is not dominated by any single interaction but by a multitude of interactions, each contributing only a small proportion of the total interaction energy. The latter is important since, as clearly illustrated by the structures of various protein-protein complexes of this PTS (this paper and refs. 15-19), not every charged residue located in the binding surface of a particular PTS protein need be involved in electrostatic interactions with complementary residues of its diverse interaction partners. While the presence of inherent redundancy does not impact specificity, it will generally result in relatively weak protein-protein interactions. In the case of the PTS, such weak interactions, which are tuned to the micro- to millimolar range, are critical to function which requires rapid dissociation of transient protein-protein complexes to permit efficient phosphoryl transfer down the reaction cascade.

Acknowledgments — We thank Frank Delaglio and Dan Garrett for software support, and Junji Iwahara and Chun Tang for many helpful discussions.

REFERENCES

1. Kundig, W., Ghosh, S., and Roseman, S. (1964) *Proc. Natl. Acad. Sci. U.S.A.* **52**, 1067-1074.
2. Postma, P. W., Lengeler, J. W., and Jacobson, G. R. (1996) *In Escherichia coli and Salmonella: Cellular and Molecular Biology* (Neidhardt, F. C., ed.), pp. 1149-1174, ASM Press, Washington DC.
3. Robillard, G. T., and Broos, J. (1999) *Biochim. Biophys. Acta* **1422**, 73-104.
4. Tchieu, J. H, Norris, V., Edwards, J. S., and Saier, M. H. (2001) *J. Mol. Microbiol. Biotechnol.* **3**, 329-346.
5. Liao, D. -I., Kapadia, G., Reddy, P., Saier, M. H. Jr.,, Reizer, J., and Herzberg, O. (1991) *Biochemistry 30*, 9583-9594.
6. Worthylake, D., Meadow, N. D., Roseman, S., Liao, D. -I., Herzberg, O., and Remington, S. J. (1991) *Proc. Natl. Acad. Sci. U.S.A.* **88**, 10382-10386.
7. Nunn, R.S., Markovic-Housley, Z., Genovesio-Taverne, G., Flükiger, K., Rizkallah, P. J., Jansonius, J. N., Schirmer, T., and Erni, B. (1996) *J. Mol. Biol.* **259**, 502-511.
8. Sliz, P., Engelmann, R., Hengstenberg, W., and Pai, E.F. (1997) *Structure* **5**, 775-788.
9. Van Montfort, R.L., Pijning, T., Kalk, K. H., Reizer, J., Saier, M.H., Thunnissen, M. M. G. M., Robillard, G. T., and Dijkstra, B. W. (1997) *Structure* **5**, 217-225.
10. Van Montfort, R.L., Pijning, T., Kalk, K. H., Hangyi ,I., Kouwijzer, M. L. C. E., Robillard, G. T., and Dijkstra, B.W. (1998) *Structure* **6**, 377-388.
11. AB, E., Schuurmann-Wolters, G., Reizer, J., Saier, M. H., Dijkstra, K., Scheek, R. M., and Robillard, G. T. (1997) *Protein Sci.* **6**, 304-314.
12. AB, E., Schuurman-Wolters, G. K., Nijlant, D., Dijkstra, K., Saier, M. H., Robillard, G. T., and Scheek, R.M. (2001) *J. Mol. Biol.* **308**, 993-1009.
13. Schauder, S., Nunn, R. S., Lanz, R., Erni, B., and Schirmer, T. (1998) *J. Mol. Biol.* **276**, 591-602.
14. Legler, P. M., Cai, M., Peterkofsky, A., and Clore, G. M. (2004) *J. Biol. Chem.* **279**, 39115-39121.
15. Cai, M., Williams, D. C., Wang, G., Lee, B. R., Peterkofsky, A., and Clore, G. M. (2003) *J. Biol. Chem.* **278**, 25191-25206.
16. Garrett, D. S., Seok, Y. -J., Peterkofsky, A., Gronenborn, A. M., and Clore, G. M. (1999) *Nature Struct. Biol.* **6**, 166-173.
17. Wang, G., Louis, J. M., Sondej, M., Seok, Y. -J.., Peterkofsky, A., and Clore, G. M. (2000) *EMBO J.* **19**, 5635-5649.
18. Cornilescu, G., Lee, B. R., Cornilescu, C. C., Wang, G., Peterkofsky, A., and Clore, G. M. (2002) *J. Biol. Chem.* **277**, 42289-42298.
19. Williams, D. C., Cai. M., Suh, J. -Y., Peterkofsky, A., and Clore, G. M. (2005) *J. Biol. Chem.* **280**, 20775-20784.
20. Otten, R., van Lune, F. S., Dijkstra, K., and Scheek, R. M. (2004) *J. Biomol. NMR* **30**, 461-462.
21. Suh, J. -Y., Tang, C., Cai, M., and Clore, G. M. (2005) *J. Mol. Biol.* **353**, 1129-1136.
22. Delaglio, F., Grzesiek, S., Vuister, G. W., Zhu, G., Pfeifer, J., and Bax, A. (1995) *J. Biomol. NMR* **6**, 277-293.
23. Garrett, D. S., Powers, R., Gronenborn, A. M., and Clore, G. M. (1991) *J. Magn. Reson.* **95**, 214-220.
24. Clore, G. M., and Gronenborn, A. M. (1991) *Science* **252**, 1390-1399.
25. Bax, A., and Grzesiek, S. (1993) *Acc. Chem. Res.* **26**, 131-138.
26. Clore, G. M., and Gronenborn, A. M. (1998) *Trends Biotech.* **16**, 22-34.
27. Bax, A., Vuister, G. W., Grzesiek, S., Delaglio, F., Wang,, A. C., Tschudin, R., and Zhu, G. (1994) *Methods Enzymol.* **239**, 79-105.
28. Saas, H. J., Musco, G., Stahl, S. J., Wingfield, P. T., and Grzesiek, S. (2000) *J. Biomol. NMR* **18**, 303-309
29. Clore, G. M., Gronenborn, A. M., Nilges, M., and Ryan, C. A. (1987) *Biochemistry* **26**, 8012-8023.
30. Schwieters, C. D., and Clore, G. M. (2001) *J. Magn. Reson.* **152**, 288-302.
31. Schwieters, C. D., Kuszewski, J., Tjandra, N., and Clore, G. M. (2003) *J. Magn. Reson. 160*, 66-74.
32. Nilges, M., Gronenborn, A. M., Brünger, A.T., and Clore, G. M. (1988) *Protein Eng.* **2**, 27-38.
33. Clore, G. M., and Kuszewski, J. (2002) *J. Am. Chem. Soc.* **124**, 2866-2867.
34. Kuszewski, J., Gronenborn, A. M., and Clore, G. M. (1999) *J. Am. Chem. Soc.* **121**, 2337-2338.
35. Schwieters, C. D., and Clore, G. M. (2001) *J. Magn. Reson.* **149**, 239-244.
36. Carson, M. (1991) *J. Appl. Crystallogr.* **24**, 958-961.
37. Nicholls, A., Sharp, K. A., and Honig, B. (1991) *Proteins 11*, 281-296.

38. Schwieters, C. D., and Clore, G.M. (2002) *J. Biomol. NMR* **23**, 221-225.
39. Van Weeghel, R. P., Meyer, G. H., Pas, H. H., Keck, W., and Robillard, G.T. (1991) *Biochemistry* **30**, 9478-9485.
40. Lolkema, J. S., Kuiper, H., ten Hoeve-Duurkens, R. H., and Robillard, G. T. (1993) *Biochemistry* **32**, 1396-1400.
41. Cantor, C. R., and Schimmel, P. R. (1980) in *Biophysical Chemistry Part III: The Behavior of Biological Macromolecules*, Chapter 18, pp. 979-1018, W. H. Freeman & Co, San Francisco.
42. van Montfort, B. A., Schuurman-Wolters, G. K., Wind, J., Broos, J., Robillard, G. T., and Poolman, B. (2002) *J. Biol. Chem.* **277**, 14717-14723.
43. Boer, H., ten Hoeve-Duurkens, R. H., and Robillard, G. T. (1996) *Biochemistry* **35**, 12901-12908.
44. Clore, G. M., and Garrett, D. S. (1999) *J. Am. Chem. Soc.* **121**, 9008-9012.
45. Williams, D. C., Cai, M., and Clore, G. M. (2004) *J. Biol. Chem.* **279**, 1449-1457.
46. Bax, A., Kontaxis, G., and Tjandra, N. (2001) *Methods Enzymol.* **339**, 127-174.
47. Jain, N. U., Wyckoff, T. J., Raetz, C. R. and Prestegard, J. H. (2004) *J. Mol. Biol.* **343**, 1379-1389.
48. Altschul, S. F., Gish, W., Liller, W., Myers, E. W., and Lipman, D. J. (1990) *J. Mol. Biol.* **215**, 403-410.
49. Jones, S., and Thornton, J. M. (1996) *Proc. Natl. Acad. Sci. U. S. A.* **93**, 13-20.
50. Ikura, M, Clore, G. M., Gronenborn, A. M., Zhu, G., Klee, C. B., and Bax, A. (1992) *Science* **256**, 632-638.
51. Laskowski, R. A., MacArthur, M. W., Moss, D. S., and Thornton, J. M. (1993) *J. Appl. Crystallogr.* **26**, 283-291.

FOOTNOTES

*This work was supported by the intramural program of NIDDK, NIH and the Intramural AIDS Targeted Antiviral Program of the Office of the Director of the National Institutes of Health (to G.M.C.).

The atomic coordinates and NMR experimental restraints (accession code 2FEW) have been deposited in the Protein Data Bank, Research Collaboratory for Structural Bioinformatics, Rutgers University, New Brunswick, NJ (http://www.rcsb.org/)

‡To whom correspondence should be addressed: Laboratory of Chemical Physics, Building 5, Rm B1-30I, NIDDK, National Institutes of Health, Bethesda, MD 20892-0520. Tel: 301-496-0782; Fax: 301-496-0825; E-mail: mariusc@intra.niddk.nih.gov.

[1]The abbreviations used are: PTS, phosphoenolpyruvate:sugar phosphotransferase system; enzyme I, EI; HPr, histidine-containing phosphocarrier protein; II^{Mtl}, the mannitol transporter; Mtl, mannitol, Man, mannose; Glc, glucose; Chb, chitobiose; NOE, nuclear Overhauser effect; HSQC, heteronuclear single quantum coherence; rms, root mean square; RDC, residual dipolar coupling.

Figure legends

Fig. 1. Binding of IIA^{Mtl}(H554Q) and phosphoIIB^{Mtl}(*C384S*). Backbone amide chemical shift perturbations upon titrating unlabeled phosphoIIB^{Mtl}(*C384S*) into a solution of 0.6 mM ^{15}N-labeled IIA^{Mtl}(H554Q) are shown by open symbols (and solid lines) and upon titrating unabeled IIA^{Mtl}(H554Q) into a solution of 0.6 mM phosphoIIB^{Mtl}(*C384S*) by closed symbols (and dashed lines). The chemical shifts were monitored using ^{1}H-^{15}N HSQC spectroscopy at a spectrometer ^{1}H frequency of 600 MHz. All the curves represent $^{1}H_N$ shift perturbations, with the exception of that for Leu-611 where the ^{15}N shift perturbation is plotted. The lines (both solid and dashed) represent non-linear least squares best-fits to all the titration data simultaneously, using a simple equilibrium binding model. The optimized value of the equilibrium dissociation constant is 3.7±0.2 mM. Residues of phosphoIIB^{Mtl}(*C384S*) are indicated by *italics*.

Fig. 2. Intermolecular NOEs in the IIA^{Mtl}(H554Q)-phosphoIIB^{Mtl}(*C384S*) complex. NOEs in a 3D ^{13}C-separated(F_2)/^{12}C-filtered (F_3) NOE experiment recorded in D_2O are specifically observed from protons attached to ^{13}C (in the F_1 dimension) to protons attached to ^{12}C (in the F_3 dimension). In *A*, IIA^{Mtl}(H554Q) is ^{15}N/^{13}C labeled and phosphoIIB^{Mtl}(*C384S*) is unlabeled; in *B*, phosphoIIB^{Mtl}(*C384S*) is ^{15}N/^{13}C labeled and IIA^{Mtl}(H554Q) is unlabeled. The asterisks denote residual diagonal (auto-correlation) peaks arising from the labeled partner. (Note ^{13}C-decoupling is not employed in the F_3 acquisition dimension and hence residual auto-correlation peaks are split into

two components separated by ~130 Hz corresponding to the $^{1}J_{CH}$ coupling; similarly, any incompletely suppressed cross-peaks arising from very high intensity intramolecular NOEs within the labeled partner will also be split by ~130 Hz and are therefore easily distinguishable from intermolecular NOEs; ref. 50). Residues of phosphoIIB^{Mtl}(*C384S*) are labeled in *italics*.

Fig. 3. Solution structure of the IIA^{Mtl}(H554Q)-phosphoIIB^{Mtl}(*C384S*) complex. *A*, Superposition of the backbone atoms of the final 200 simulated annealing structures. The backbone (N, Cα, C atoms) of IIA^{Mtl}(H554Q) is shown in blue and that of phosphoIIB^{Mtl}(*C384S*) in *green*. The active site residues, Gln554 and *phospho-Ser384* are shown in *red* and *gold*, respectively. *B*, Isosurface of the reweighted atomic density probability map for some interfacial side-chains in the vicinity of the active sites on the two proteins. The isosurface calculated from the ensemble of 200 simulated annealing structures (drawn at a value of 25% maximum) and side-chain coordinates for the restrained regularized mean structure are shown in *red* for IIA^{Mtl}(H554Q) and in *purple* for phosphoIIB^{Mtl}(*C384S*). The relevant portions of the backbone are represented as *blue* and *green* tubes for IIA^{Mtl}(H554Q) and phosphoIIB^{Mtl}(C384S), respectively. Residues of phosphoIIB^{Mtl}(*C384S*) are labeled in *italics*.

Fig. 4. Overall view of the IIA^{Mtl}(H554Q)-phosphoIIB^{Mtl}(*C384S*) complex. Two approximately orthogonal views of the complex are displayed in a ribbon diagram representation with IIA^{Mtl}(H554Q) in *blue* and phosphoIIB^{Mtl}(*C384S*) in *green*. The side-chains of the two active site residues, Gln-554 and *phosphoSer-384* are depicted in red and gold, respectively. Residues of phosphoIIB^{Mtl}(*C384S*) are labeled in *italics*.

Fig. 5. The IIA^{Mtl}(H554Q)-phosphoIIB^{Mtl}(*C384S*) interface. *A*, Overall stereoview of the interface. *B*, Close-up depicting the insertion of Met393 of phosphoIIB^{Mtl}(*C384S*) into a deep hydrophobic pocket on IIA^{Mtl}(H554Q). *C*, Close-up in the vicinity of the active sites of the two proteins. The color coding for IIA^{Mtl}(H554Q) and phosphoIIB^{Mtl}(*C384S*) is as follows: backbone (shown as a transparent tubes in *A* and transparent ribbons in *B* and *C*), *blue* and green, respectively; and side-chain bonds, *red* and *gray*, respectively. The side-chain bonds of the two active site residues, Gln-554 and *phosphoSer-384*, are in *gold*. The side-chain atoms are colored according to atom type; carbon, *cyan*; nitrogen, *blue*; oxygen, *red*; sulphur, *yellow*; and phosphorus, *grey*. Residues of phosphoIIB^{Mtl}(*C384S*) are labeled in *italics*.

Fig. 6. Comparison of the interaction surfaces for the IIA^{Mtl}(H554Q)-phosphoIIB^{Mtl}(*C384S*) and IIA^{Mtl}-HPr complexes. A, IIA^{Mtl}(H554Q)·phosphoIIB^{Mtl}(*C384S*), and *B*, IIA^{Mtl}-HPr. The top panels display the interaction surface on IIA^{Mtl} for (*A*) IIB^{Mtl} and (*B*) HPr; the bottom panels depict the interaction surfaces on (*A*) IIB^{Mtl} and (*B*) HPr for IIA^{Mtl}. The surfaces are color coded as follows: hydrophobic residues, *green*; uncharged residues bearing a polar functional group, *cyan*; negatively charged residues, *red*; positively charged residues, *blue*; active site histidines (or glutamine) (His/Gln-554 for IIA^{Mtl} and *His-15* for HPr), *purple*; active site *phosphoSer-384* of IIB^{Mtl}, *yellow*. Relevant portions of the backbone and active site residue of the interacting partner are displayed as tubes and bonds, respectively. Also shown in the top panel of (*A*) are the side chains of *Met-388* and *Met-383* in *gold* illustrating how their methyl group point directly into deep hydrophobic pockets on the surface of IIA^{Mtl}. Residues of phosphoIIB^{Mtl}(*C384S*) and HPr are labeled in *italics*. The coordinates of the IIA^{Mtl}-HPr complex are taken from ref. 18.

Fig. 7. Diagrammatic representation of the intermolecular contacts between IIA^{Mtl} and its partner proteins, IIB^{Mtl} and HPr. Residues of IIB^{Mtl} and HPr involved in electrostatic interactions with a residue on IIA^{Mtl} are colored *red*. For IIA^{Mtl}, residues that are involved in interactions with both IIB^{Mtl} and HPr are colored *green*, while residues that only interact with one of the two partner proteins are colored *blue*. The active site residues, His/Gln-554 of IIA^{Mtl}, *phosphoSer-384* of IIB^{Mtl} and *His15* of HPr are colored *purple*. Residues of phosphoIIB^{Mtl}(*C384S*) and HPr are labeled in *italics*. The contacts between IIA^{Mtl} and HPr are taken from ref. 18.

Fig. 8. The phosphoryl transition state of the IIA^{Mtl}-IIB^{Mtl} complex. The backbone (tube representation) and side-chain bonds of IIA^{Mtl} are shown in *blue* and *red*, respectively; the backbone (tube representation) and side-chain bonds of IIB^{Mtl} are shown in *green* and *gray*, respectively. The side-chain bonds of the His-554---P---Ser-384 transition state are shown in *gold*. Minimal changes in coordinates in the immediate vicinity of the active site residues are required to accommodate the transition state. The coordinates of the post-transition state complex that shift to form the transition state are shown as transparent bonds (side-chains of *phosphoSer-384*, *Met-388*, Arg-438

and Gln-554; and tubes (backbone of residues *382-384* and 553-555). Residues of phosphoIIB^{Mtl}(*C384S*) are labeled in *italics*.

Fig. 9. Proposed mechanism of phosphoryl transfer between IIA^{Mtl} and IIB^{Mtl}. The interactions stabilizing the phsophoryl group in phosphoIIA^{Mtl} are modled based on the crystal structure of IIA^{Mtl} (10). The hydrogen bonding interactions stabilizing the thiolate state of *Cys-384* of IIB^{Mtl} are taken from the NMR structure of IB^{Mtl} (14). The hydrogen bonding interactions stabilizing the phosphoryl group in phosphoIIB^{Ml} are taken from the NMR structure of phosphoIIB^{Mtl} (21). The hydrogen bonding interactions depicted in the post-transition state IIA^{Mtl}-phosphoIIB^{Mtl} complex and the phosphoryl transition state are taken from the present work. Intramolecular and intermolecular hydrogen bonds are depicted by *blue* and *red* dashed lines, respectively.

Table I

Structural statistics

The notation of the NMR structures are as follows: <SA> are the final 270 simulated annealing structures, $(SA)_r$ is the restrained regularized mean structure.

	<SA>	$\overline{(SA)_r}$
Number of experimental NMR restraints		
Intermolecular interproton distance restraints	84	
IIA^{Mtl} intramolecular interproton distance restraints[a]	37	
IIB^{Mtl} intramolecular interproton distance restraints[a]	46	
IIA^{Mtl} interfacial sidechain torsion angle restraints	36	
IIB^{Mtl} interfacial sidechain torsion angle restraints	19	
R.m.s. deviation from interproton distance restraints (Å)[b]	0.012±0.031	0.009
R.m.s. deviation from sidechain torsion angle restraints (°)[b]	0.007±0.001	0.31
Measures of structural quality[c]		
Intermolecular repulsion energy ($kcal \cdot mol^{-1}$)	3.8±0.9	6.5
Intermolecular Lennard-Jones energy ($kcal \cdot mol^{-1}$)	-31.2±3.1	-36.7
Coordinate precision of the complex (Å)[d]		
Complete backbone (N, Cα, C', O) atoms	0.10	
Interfacial sidechain heavy atoms	0.65	

[a]The intramolecular NOE-derived interproton distance restraints relate only to interfacial sidechains.

[b]None of the structures exhibit interproton distance violations >0.3 Å or torsion angle violations >5°.

[c]The intermolecular repulsion energy is given by the value of the quartic van der Waals repulsion term calculated with a force constant of 4 $kcal \cdot mol^{-1} \cdot Å^{-4}$ and a van der Waals radius scale factor of 0.78. The intermolecular Lennard-Jones van der Waals interaction energy is calculated using the CHARMM19/20 parameters and is *not* included in the target function used to calculate the structures.

[d]Defined as the average r.m.s. difference between the final 270 simulated annealing structures and the mean coordinates. The value quoted for the complete backbone provides only a measure of the precision with which the orientation and translation of the two proteins in the complex have been determined, and does not take into account the backbone accuracy of the X-ray/NMR coordinates of IIA^{Mtl} and the NMR coordinates of $phosphoIIB^{Mtl}$ used for conjoined rigid body/torsion angle dynamics docking. The accuracy of the X-ray coordinates of IIA^{Mtl} (including NMR refinement of the four variable regions comprising residues 540-543, 555-567, 580-585 and 593-599 on the basis of backbone RDCs) is likely to be around 0.3 Å judging from the crystallographic resolution and R-factor (10), as well as the dipolar coupling R-factors (this paper). The accuracy of the restrained regularized mean coordinates of $phosphoIIB^{Mtl}$ can be estimated from the coordinate precision (0.3 Å) and the values of 14-16% for cross-validated N-H dipolar coupling R-factors in two alignment media (phage pf1 and neutral polyacrylamide gel; ref. 21) which suggest that the coordinate accuracy is comparable to a 1.5-2 Å resolution crystal structure (19,45). The percentage residues in the most favored region of the Ramachandran map (51) is 92% for IIA^{Mtl} and 91% for $phosphoIIB^{Mtl}$.

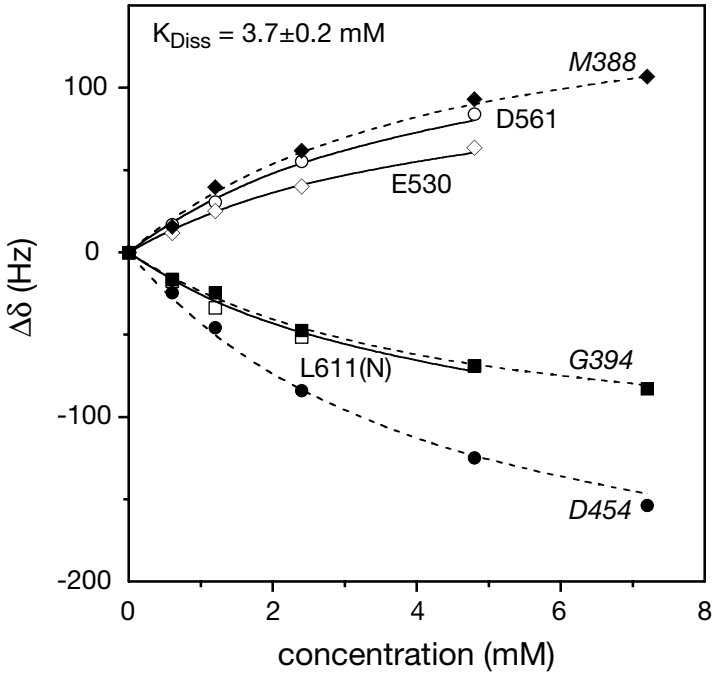
K_Diss = 3.7±0.2 mM
M388
D561
E530
G394
L611(N)
D454
100
0
-100
-200
Δδ (Hz)
0
2
4
6
8
concentration (mM)

Fig. 1

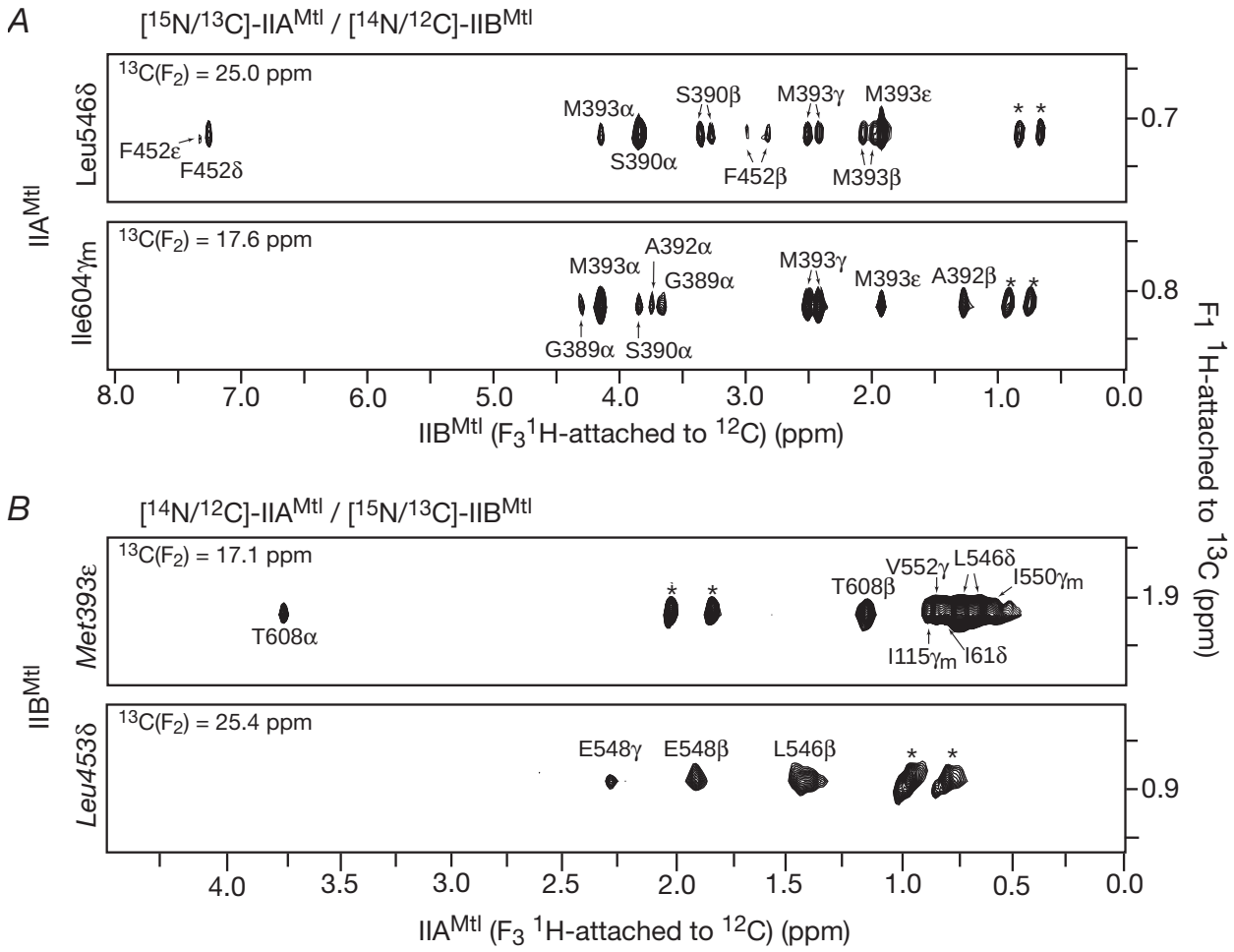
A
[15N/13C]-IIAMtl / [14N/12C]-IIBMtl
13C(F2) = 25.0 ppm
Leu546δ
M393α
S390β
M393γ
M393ε
F452ε
F452δ
S390α
F452β
M393β
0.7
IIAMtl
13C(F2) = 17.6 ppm
Ile604γm
A392α
M393α
G389α
M393γ
M393ε
A392β
0.8
G389α
S390α
8.0
7.0
6.0
5.0
4.0
3.0
2.0
1.0
0.0
IIBMtl (F3 1H-attached to 12C) (ppm)
F1 1H-attached to 13C (ppm)
B
[14N/12C]-IIAMtl / [15N/13C]-IIBMtl
13C(F2) = 17.1 ppm
Met393ε
V552γ
L546δ
T608β
I550γm
1.9
T608α
I115γm
I61δ
IIBMtl
13C(F2) = 25.4 ppm
Leu453δ
E548γ
E548β
L546β
0.9
4.0
3.5
3.0
2.5
2.0
1.5
1.0
0.5
0.0
IIAMtl (F3 1H-attached to 12C) (ppm)

Fig. 2

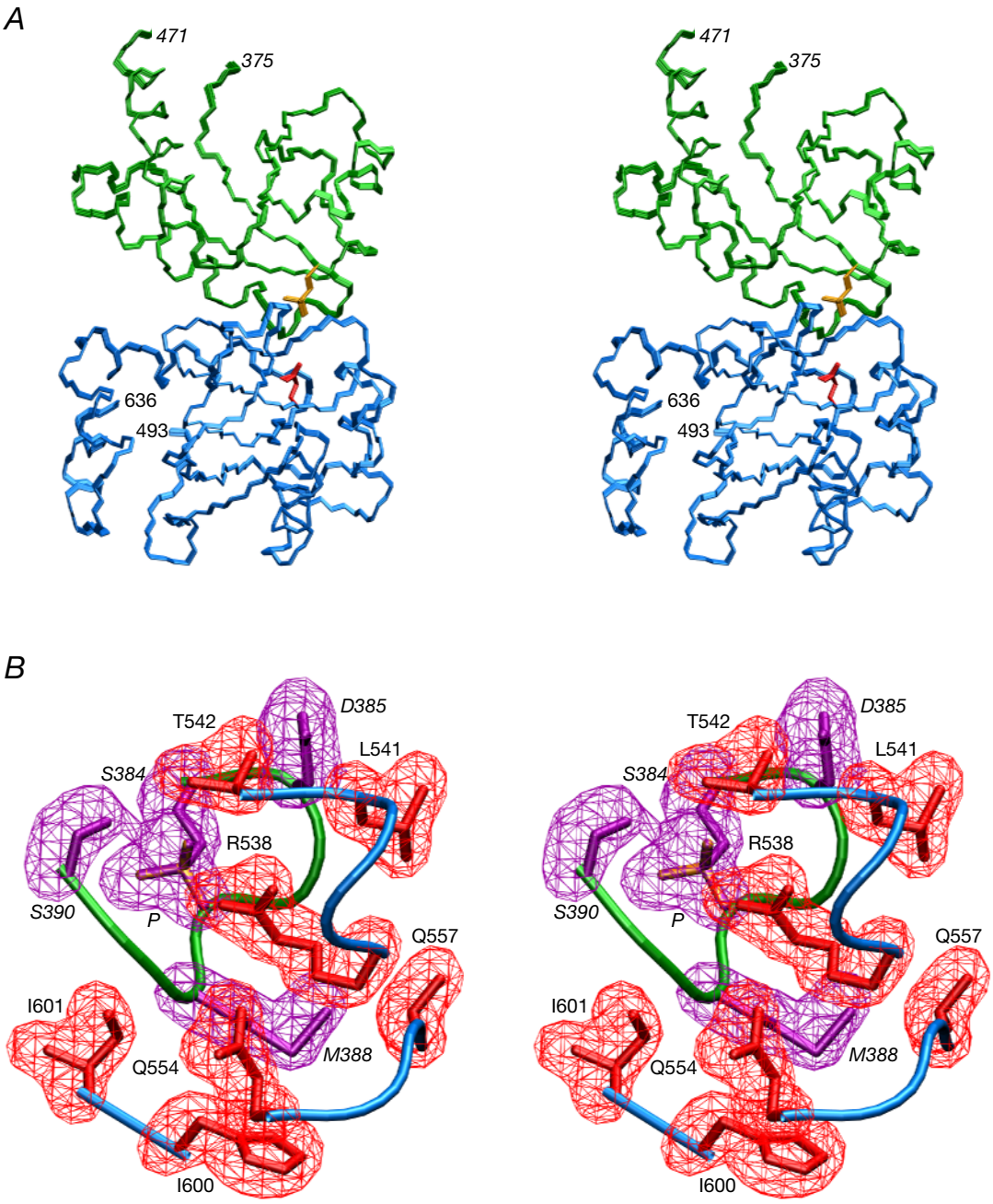
A
471
375
636
493
471
375
636
493
B
T542
D385
L541
S384
R538
S390
P
Q557
I601
M388
Q554
I600
T542
D385
L541
S384
R538
S390
P
Q557
I601
M388
Q554
I600

Fig. 3

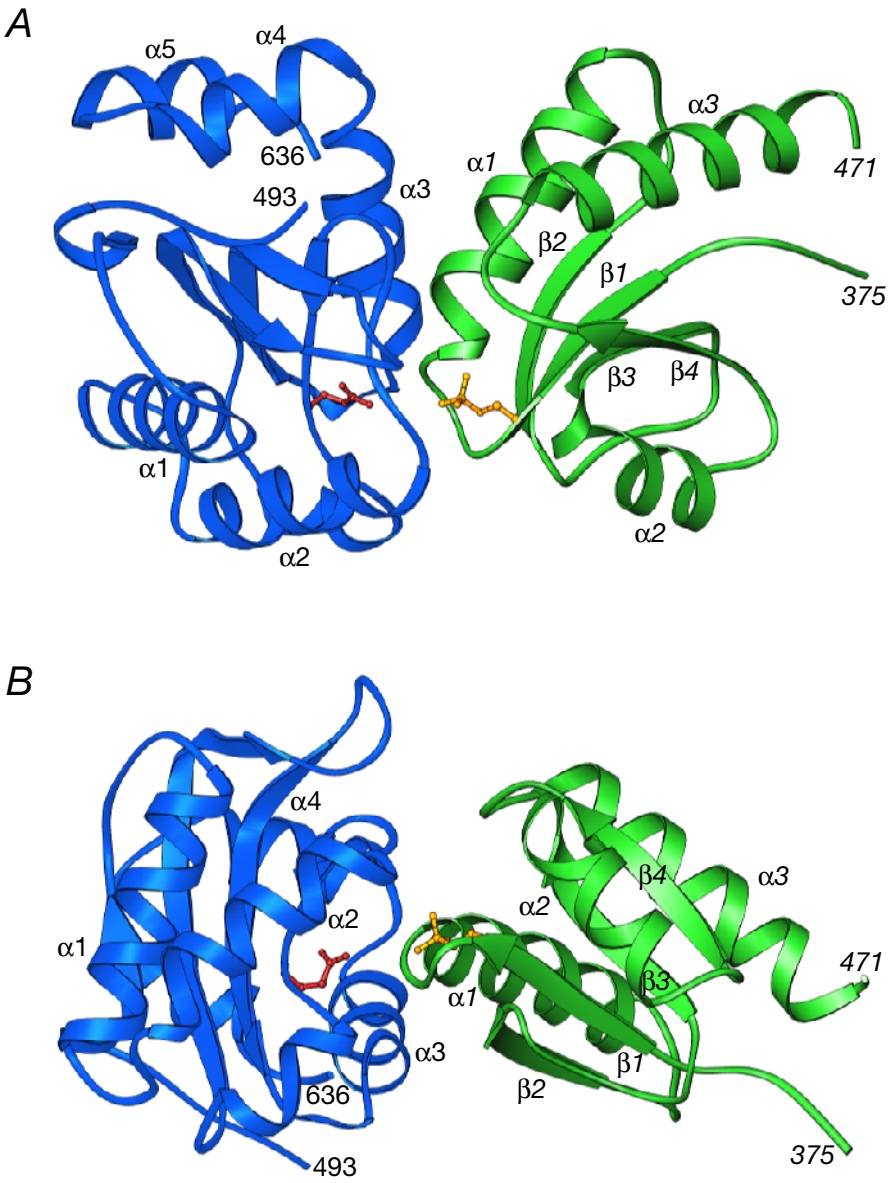
A
α5
α4
636
493
α3
α1
α2
α3
471
α1
β2
β1
375
β3
β4
α2
B
α4
α2
α1
α3
636
493
α3
β4
α2
471
β3
α1
β1
β2
375

Fig. 4

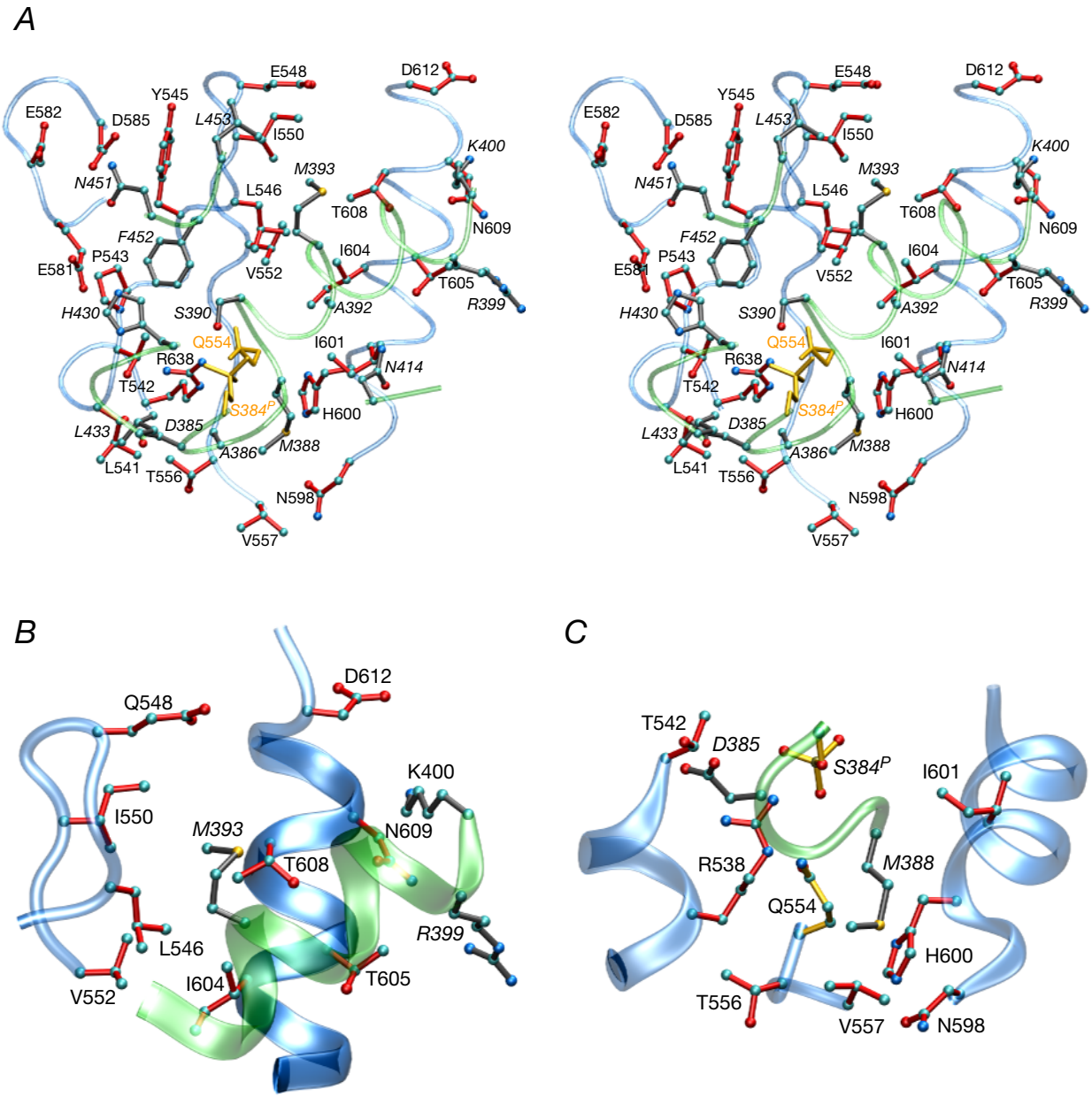
A
E548
D612
Y545
E582
D585
L453
I550
K400
M393
N451
L546
T608
N609
F452
E581
P543
V552
I604
T605
R399
H430
S390
A392
Q554
I601
R638
N414
T542
S384P
H600
D385
L433
A386
M388
L541
T556
N598
V557
B
Q548
D612
K400
I550
M393
N609
T608
R399
L546
T605
I604
V552
C
T542
D385
S384P
I601
R538
M388
Q554
H600
T556
V557
N598

Fig. 5

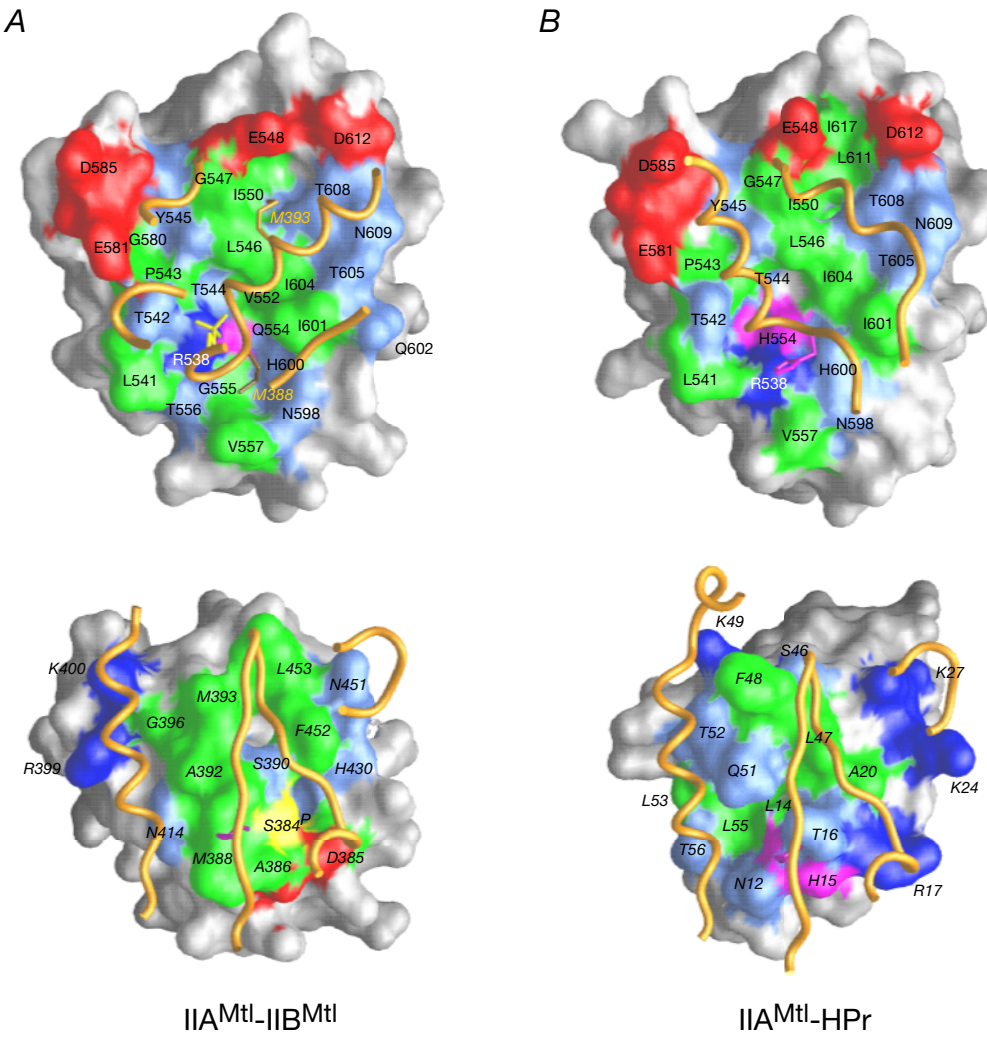
A
E548
D612
D585
G547
I550
T608
Y545
M393
N609
E581
G580
L546
P543
T605
T544
I604
V552
T542
Q554
I601
Q602
R538
H600
L541
G555
M388
T556
N598
V557
K400
L453
N451
M393
G396
F452
R399
A392
S390
H430
N414
S384
P
M388
A386
D385
IIA^Mtl-IIB^Mtl
B
E548
I617
D612
L611
D585
G547
Y545
I550
T608
N609
L546
E581
P543
T605
T544
I604
T542
I601
H554
H600
L541
R538
N598
V557
K49
S46
K27
F48
T52
L47
Q51
A20
K24
L53
L14
L55
T16
T56
N12
H15
R17
IIA^Mtl-HPr

Fig. 6

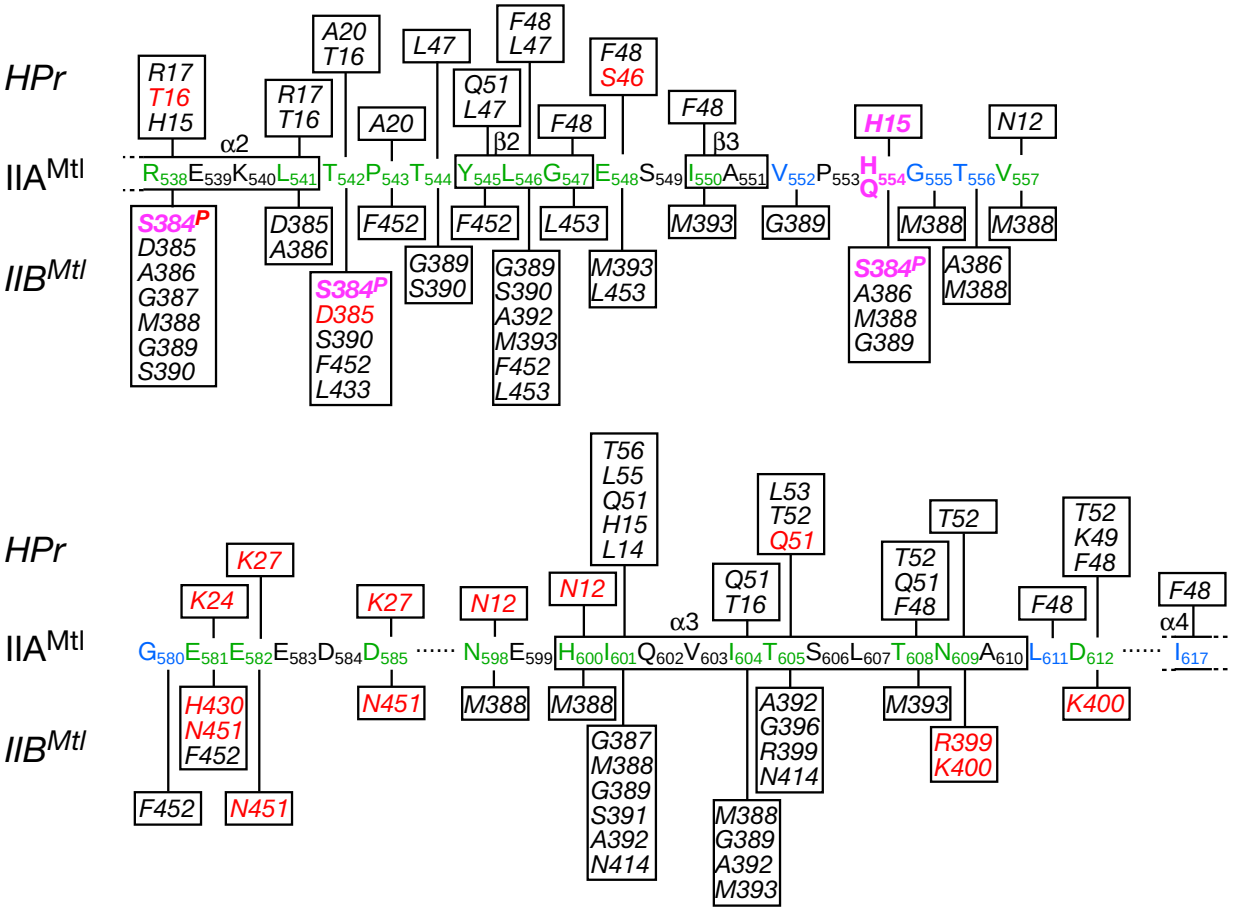
HPr
IIA^Mtl
IIB^Mtl
α2
β2
β3
α3
α4
R538 E539 K540 L541 T542 P543 T544 Y545 L546 G547 E548 S549 I550 A551 V552 P553 H554 Q554 G555 T556 V557 I617
R17 T16 H15
A20 T16
R17 T16
A20
L47
Q51 L47
F48 L47
F48
F48 S46
F48
H15
N12
S384P D385 A386 G387 M388 G389 S390
D385 A386
S384P D385 S390 F452 L433
F452
G389 S390
F452
G389 S390 A392 M393 F452 L453
L453
M393 L453
M393
G389
M388
A386 M388
S384P A386 M388 G389
M388
K27
K24
K27
N12
N12
T56 L55 Q51 H15 L14
Q51 T16
L53 T52 Q51
T52
T52 Q51 F48
T52 K49 F48
F48
F48
H430 N451 F452
N451
M388
M388
G387 M388 G389 S391 A392 N414
A392 G396 R399 N414
M388 G389 A392 M393
M393
R399 K400
K400
F452
N451

Fig. 7

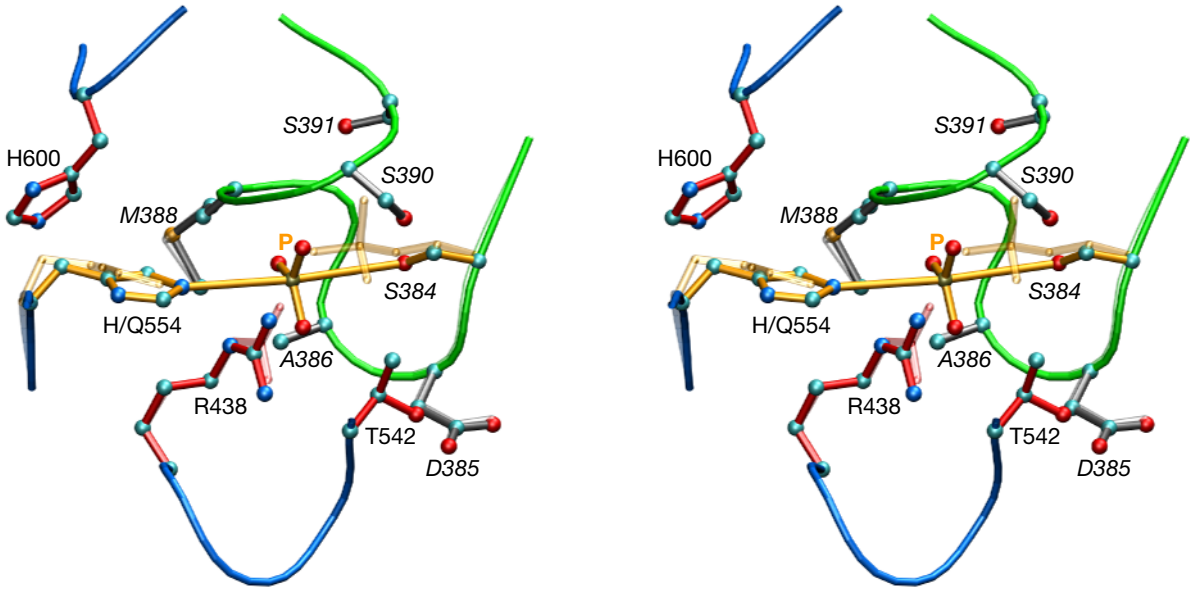
H600
S391
S390
M388
P
S384
H/Q554
A386
R438
T542
D385
H600
S391
S390
M388
P
S384
H/Q554
A386
R438
T542
D385

Fig. 8

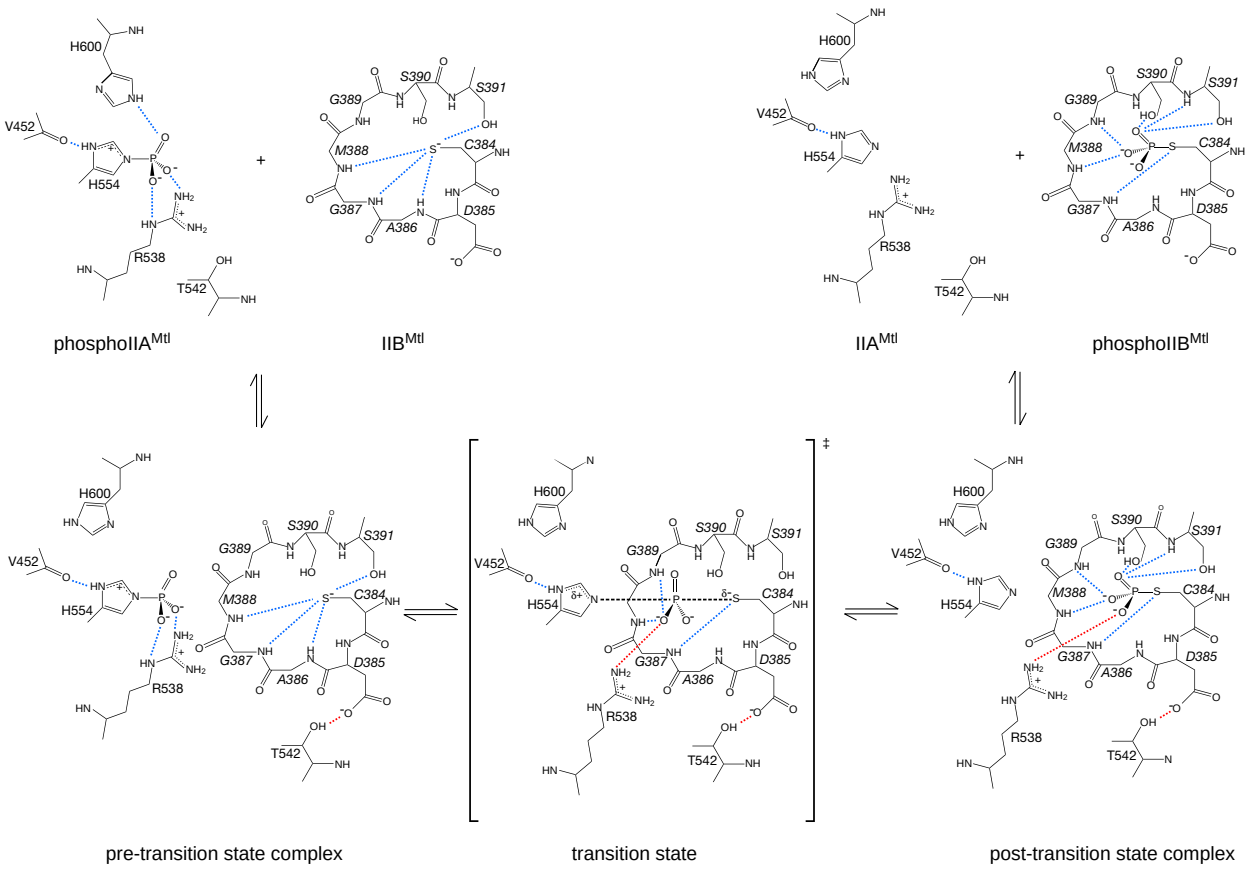
phosphoIIA^Mtl
IIB^Mtl
IIA^Mtl
phosphoIIB^Mtl
pre-transition state complex
transition state
post-transition state complex
H600
V452
H554
R538
T542
G389
S390
S391
M388
C384
G387
A386
D385

Fig. 9